

See discussions, stats, and author profiles for this publication at: <https://www.researchgate.net/publication/261441489>

Mitigating Voltage Fade in Cathode Materials by Improving Atomic Level Uniformity of Elemental Distribution.

ARTICLE *in* NANO LETTERS · APRIL 2014

Impact Factor: 13.59 · DOI: 10.1021/nl500486y · Source: PubMed

CITATIONS

38

READS

13,322

11 AUTHORS, INCLUDING:



Jianming Zheng

Pacific Northwest National Laboratory

62 PUBLICATIONS 1,488 CITATIONS

[SEE PROFILE](#)



Meng Gu

University of California, Davis

69 PUBLICATIONS 1,318 CITATIONS

[SEE PROFILE](#)



Xilin Chen

XG Sciences

54 PUBLICATIONS 1,442 CITATIONS

[SEE PROFILE](#)



Lee Pullan

FEI

17 PUBLICATIONS 509 CITATIONS

[SEE PROFILE](#)

Mitigating Voltage Fade in Cathode Materials by Improving the Atomic Level Uniformity of Elemental Distribution

Jianming Zheng,[†] Meng Gu,[‡] Arda Genc,[§] Jie Xiao,[†] Pinghong Xu,^{||} Xilin Chen,[†] Zihua Zhu,[‡] Wenbo Zhao,[‡] Lee Pullan,[§] Chongmin Wang,^{*,‡} and Ji-Guang Zhang^{*,†}

[†]Energy and Environment Directorate, Pacific Northwest National Laboratory, 902 Battelle Boulevard, Richland, Washington 99352, United States

[‡]Environmental Molecular Sciences Laboratory, Pacific Northwest National Laboratory, 902 Battelle Boulevard, Richland, Washington 99352, United States

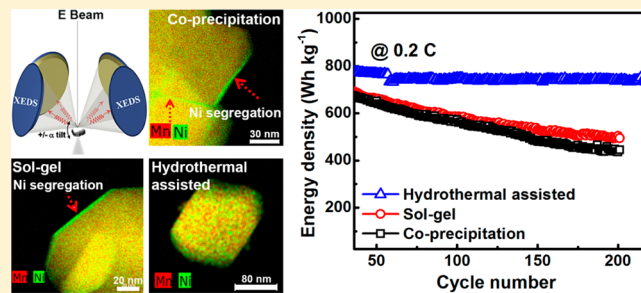
[§]FEI Company, 5350 NE Dawson Creek Drive, Hillsboro, Oregon 97124, United States

^{||}University of California, Davis, 1 Shields Ave, Davis, California 95616, United States

S Supporting Information

ABSTRACT: Lithium- and manganese-rich (LMR) layered-structure materials are very promising cathodes for high energy density lithium-ion batteries. However, their voltage fading mechanism and its relationships with fundamental structural changes are far from being well understood. Here we report for the first time the mitigation of voltage and energy fade of LMR cathodes by improving the atomic level spatial uniformity of the chemical species. The results reveal that LMR cathodes ($\text{Li}[\text{Li}_{0.2}\text{Ni}_{0.2}\text{Mn}_{0.6}]_{\text{O}_2}$) prepared by coprecipitation and sol-gel methods, which are dominated by a LiMO_2 type $R\bar{3}m$ structure, show significant nonuniform Ni distribution at particle surfaces. In contrast, the LMR cathode prepared by a hydrothermal assisted method is dominated by a Li_2MO_3 type $C2/m$ structure with minimal Ni-rich surfaces. The samples with uniform atomic level spatial distribution demonstrate much better capacity retention and much smaller voltage fade as compared to those with significant nonuniform Ni distribution. The fundamental findings on the direct correlation between the atomic level spatial distribution of the chemical species and the functional stability of the materials may also guide the design of other energy storage materials with enhanced stabilities.

KEYWORDS: Layered structure, cation distribution, Ni-rich surface, spinel formation, voltage fade, lithium ion battery



Lithium ion batteries (LIB) are receiving increasing worldwide attention for applications in electric vehicles (EV) and stationary energy storage.^{1–12} However, the limited energy density and cycle life, as well as cost and safety issues, of state-of-the-art LIB technologies still hinder their applications in long-range EV and large-scale grid applications.¹² Lithium- and manganese-rich (LMR) layered-structure cathode materials deliver a much higher energy density than traditional cathode materials such as LiMn_2O_4 spinel and LiCoO_2 .^{13–19} A typical LMR cathode (such as $\text{Li}[\text{Li}_{0.2}\text{Ni}_{0.2}\text{Mn}_{0.6}]_{\text{O}_2}$) can deliver a discharge capacity exceeding 250 mAh g⁻¹ after activation of the Ni-deficient Li_2MO_3 type $C2/m$ component²⁰ in the initial charge process, typically at ~4.5 V.^{21–23} High content substitution of Mn and Ni for expensive Co also gives rise to a significant reduction of cost. In addition, these LMR cathode materials reportedly showed good thermal stability, with the onset of thermal decomposition at 250 °C.²⁴ These excellent properties make LMR layered material one of the most promising candidates as high energy density cathodes. However, significant challenges, including voltage fade and

limited cycle life in LMR cathodes, still remain to be overcome prior to their large-scale market penetration.^{25–27}

In the literature, the coprecipitation (CP) method has been widely used to prepare LMR cathode materials because it is presumed to produce materials with a uniform cation distribution.^{18,24,28,29} Surprisingly, a selective surface lattice plane segregation of Ni ions was discovered for the typical LMR cathode material $\text{Li}[\text{Li}_{0.2}\text{Ni}_{0.2}\text{Mn}_{0.6}]_{\text{O}_2}$ prepared by the CP method, in which the Ni ions preferentially segregated at the surface facets terminated with a mix of anions and cations.³⁰ This unexpected segregation results in a higher diffusion barrier for lithium ions near the particle surface, which consequently leads to poor rate capability and fast capacity fading of LMR cathodes. As reported in earlier works, the rate capability and cyclability of the as-prepared materials are greatly affected by the degree of cation ordering and uniformity.^{16,30–32} In this regard, limitations in the properties of LMR cathode materials

Received: February 6, 2014

Revised: April 2, 2014

Published: April 7, 2014

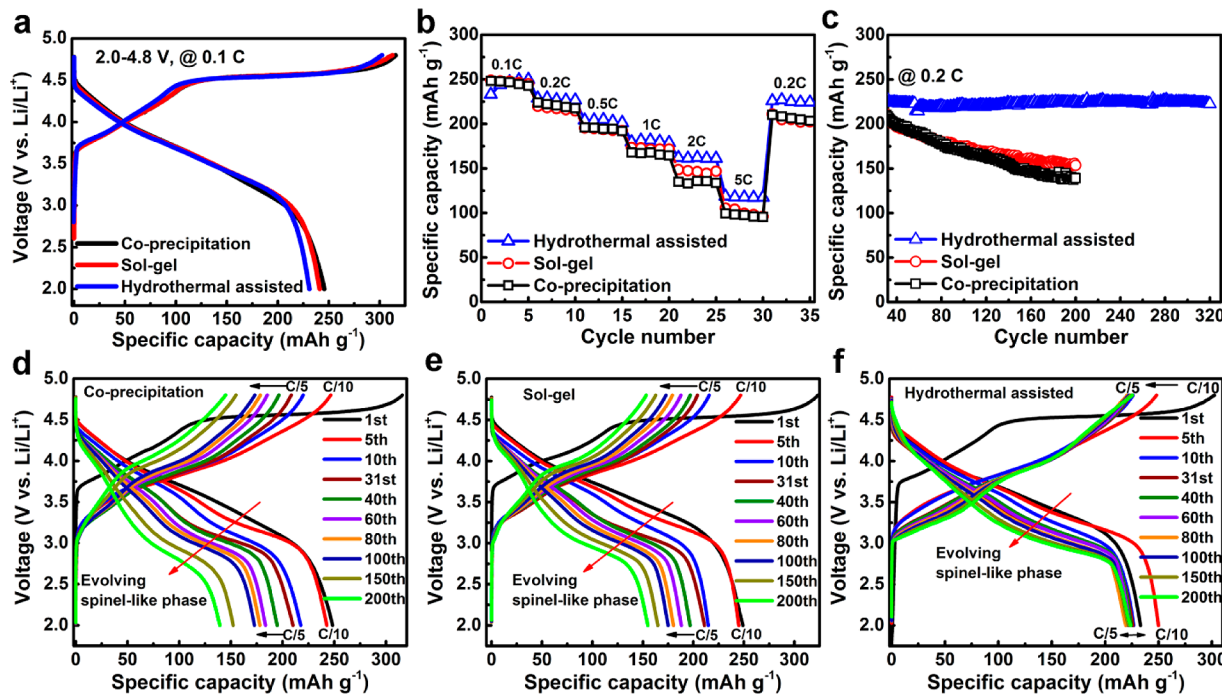


Figure 1. Charge/discharge characteristics of LMR cathodes prepared by different methods. (a) Initial charge/discharge profiles at C/10 in the voltage range of 2.0–4.8 V. (b) Comparison of rate performance. (c) Cycling performance at C/5 after rate performance tests. Corresponding charge/discharge profile evolutions of materials prepared by the (d) CP method, (e) SG method, and (f) HA method during the long-term cycling.

are largely determined by the transition metal (TM) ion Ni/Mn distribution issues in these materials. As Ni/Mn distribution is closely related with synthetic conditions applied for preparing the precursor, the optimizing synthesis process may enhance the uniformity of Ni distribution and thus improve the charge/discharge performance of the LMR cathode.

Here, we report on the direct correlation between voltage fade and atomic level spatial distribution of chemical species among LMR cathode materials ($\text{Li}[\text{Li}_{0.2}\text{Ni}_{0.2}\text{Mn}_{0.6}]_{\text{O}_2}$) prepared by several methods, including coprecipitation (CP), sol-gel (SG), and hydrothermal assisted (HA) methods. Quantitative chemical composition analysis was performed on these materials using large-area X-ray energy dispersive spectroscopy (XEDS) mapping. Meanwhile, we used aberration-corrected scanning transmission electron microscopy (STEM) to acquire detailed crystallographic data on $\text{Li}[\text{Li}_{0.2}\text{Ni}_{0.2}\text{Mn}_{0.6}]_{\text{O}_2}$ cathode prepared by different methods. The atomic contrast in high-angle annular dark field (HAADF) STEM imaging identified the details of stacking and ordering in the particles. We found that the materials prepared by the CP and SG methods exhibit a relatively high propensity of nonuniform Ni distribution, leading to fast voltage fade and poor cycling stability. However, the material prepared by the HA method exhibits a uniform Ni distribution and greatly reduced voltage fade. To the best of our knowledge, this is the first direct atomic-scale evidence to correlate atomic level cation uniformity with the electrochemical performance of cathode materials.

The electrochemical performances of $\text{Li}[\text{Ni}_{0.20}\text{Li}_{0.20}\text{Mn}_{0.60}]_{\text{O}_2}$ cathodes prepared by different methods were evaluated in conventional carbonate-based electrolyte (1 M $\text{LiPF}_6/\text{EC} + \text{DMC}$), and the initial charge/discharge profiles at C/10 rate are shown in Figure 1a. The slope charging voltage region below 4.45 V is attributed to lithium ion deintercalation associated with the oxidation of Ni^{2+} to Ni^{3+} and then to Ni^{4+} ,

while the subsequent voltage plateau at ~4.5 V, which is beyond the formal oxidation potential of Ni^{2+} to Ni^{4+} , could be assigned to the removal of lithium ions concomitant with an irreversible loss of oxygen from the Ni-deficient Li_2MO_3 type $\text{C}2/m$ component (M is Mn(major)/Ni(minor)),²⁰ based on in situ X-ray diffraction studies and differential electrochemical mass spectrometry (DEMS) results.^{13,16,33} Within the oxygen loss plateau, the Li_2MO_3 component ($\text{C}2/m$ structure with monoclinic symmetry) is activated, and thus the material can deliver a high capacity during the subsequent discharge process. After activation of the Li_2MO_3 component, the three materials deliver similar discharge capacities approaching 250 mAh g^{-1} . For HA material, the charge capacity below 4.45 V is only 103 mAh g^{-1} , which is ~10% below those extracted from the CP material (113 mAh g^{-1}) and the SG material (112 mAh g^{-1}), implying a lower content of active Ni^{2+} available during lithium ion extraction in this voltage region.

The rate capability of LMR cathode materials prepared by different methods is compared in Figure 1b. These materials show similar discharge capacities at current rates lower than 0.5 C. However, at current rates higher than 1.0 C, the discharge capacities start to deviate from each other for different materials. The HA material shows the highest reversible capacity of 119 mAh g^{-1} at the 5C rate, which is ~20% higher than those delivered by the CP and SG materials. It is believed that the improved rate capability can be attributed to a stable electrode structure during cycling. After the rate capability test, the cells were further cycled at C/5, and the result is demonstrated in Figure 1c. Both CP and SG materials display fast capacity degradation during cycling at C/5, while the HA material shows excellent cycling stability. The discharge capacities fade rapidly to 139 and 153 mAh g^{-1} , respectively, for CP and SG materials after 200 cycles. The stability of the HA material could be first evidenced by the recovery of a discharge capacity of 226 mAh g^{-1} at C/5 after the high rate

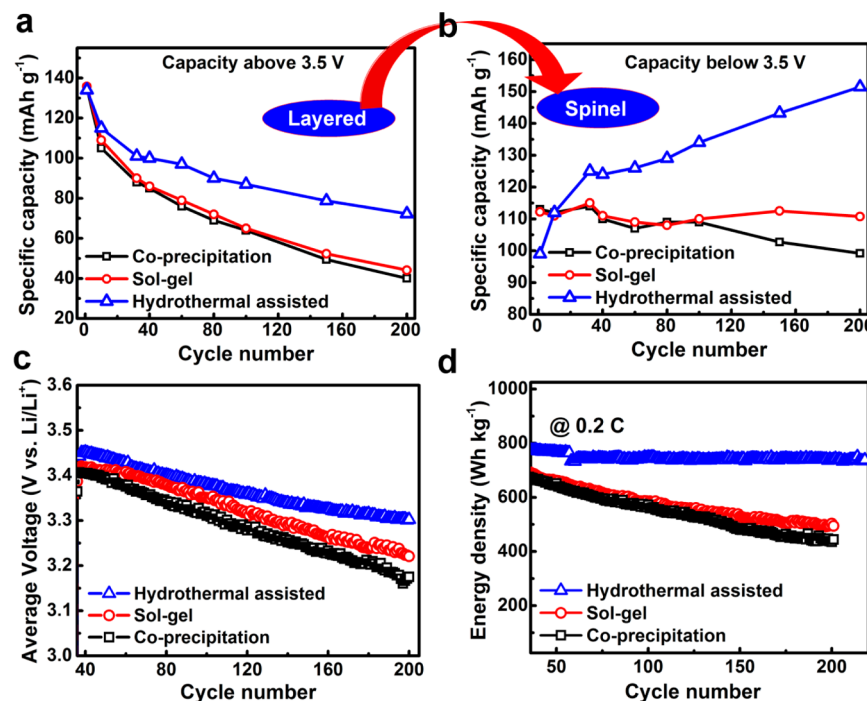


Figure 2. Electrochemical evolutions of LMR cathodes prepared by different methods during cycling. (a) Discharge capacity above 3.5 V during cycling; (b) discharge capacity below 3.5 V during cycling. (c) Average discharge voltage as a function of cycle number during cycling at C/5. (d) Energy density as a function of cycle number during cycling at C/5.

discharge at 5 C, which is higher than those for the other two materials. More importantly, the HA material exhibits no identifiable capacity degradation over 300 cycles. To further confirm the good structural stability of the HA material, we also cycled the HA material at the low current density of C/10, which means increased residing time at high voltage (>4.4 V) and a greater chance of side reactions. Even at the low current density, there is no capacity decay up to 90 cycles in spite of the high charge cutoff voltage of 4.8 V (Figure S1 in the Supporting Information). All of these results demonstrate the excellent cycle life and rate capability of HA material, thus validating HA material as a promising cathode material for sustainable operation.

Figure 1d–f shows the charge/discharge profile evolutions for $\text{Li}[\text{Ni}_{0.20}\text{Li}_{0.20}\text{Mn}_{0.60}] \text{O}_2$ materials during the long-term cycling test. The CP and SG materials display severe voltage fade on cycling, as indicated by the red arrow in Figure 1d and e. There are two aspects contributing to voltage fade of LMR cathode materials during cycling. Obviously, the electrode polarization caused by the deterioration of electrode/electrolyte interface associated with the side reactions between the electrode and the electrolyte at high voltages can result in voltage fade during discharge process. However, the primary reason for the voltage fade should be ascribed to the intrinsic gradual structural evolution from layered to spinel-like phase during repeated cycling, as observed for other layered materials with Li_2MO_3 character.^{34,35} In principle, layered-to-spinel transformation involves migration of TM ions into Li sites and Li ions into tetrahedral sites followed by a distortion of oxygen lattices. With the extensive removal of Li ions at high voltage, migration of the TM ions into the Li layer via the adjacent tetrahedral sites is energetically favorable and thus could facilitate the formation of a spinel-like phase.²⁸ This phase transformation leads to a structure featuring layered-spinel intergrowth. However, there is an apparent absence of a

strong redox reaction peaks at ~4.0 V that corresponds to the removal of lithium ions from the tetrahedral sites of an evolving spinel-like component. This discrepancy is tentatively ascribed to the complicated cation arrangement within the layered-spinel intergrown structure that limits the lithium ion insertion/extraction reactions to be predominantly associated with the filling/evacuating of octahedral sites rather than tetrahedral sites.³⁴ Consequently, only the evolution of a redox reaction in the ~3.0 V region is observed after cycling. In addition, the lithium ion intercalation/deintercalation redox reactions of conventional layered structure component $\text{LiNi}_{0.5}\text{Mn}_{0.5}\text{O}_2$ mainly occur at voltage higher than 3.5 V.³⁶ Therefore, in this study, the discharge capacity below 3.5 V is mainly ascribed to lithium ion insertion into the evolved spinel-like structure, consistent with literature report.³⁷ Due to the phase transformation, the discharge capacity above 3.5 V decreases monotonously during cycling as shown in Figure 2a. Ideally, this decrease should be accompanied by an increase of discharge capacity below 3.5 V due to increased formation of the spinel-like phase. However, the CP and SG material exhibit continuous capacity decay below 3.5 V, implying a deteriorated structure for lithium ion storage.

In contrast to the CP and SG materials, the HA material shows much less voltage fade during cycling (Figure 1f). It also exhibits a significantly reduced capacity decay above 3.5 V (Figure 2a), revealing a suppression of the evolving spinel-like component, and a capacity increase in the region below 3.5 V (Figure 2b), which is consistent with the capacity compensation predicted above. The capacity increase in the lower voltage region (<3.5 V) is very close to the capacity decrease in the higher voltage region (>3.5 V), leading to an excellent capacity retention, as shown in Figure 1c. Galvanostatic intermittent titration technique (GITT) analysis further substantiates the stability of the lithium ion diffusion coefficients (D_{Li^+}) for HA material during cycling (Figure S2 in the Supporting

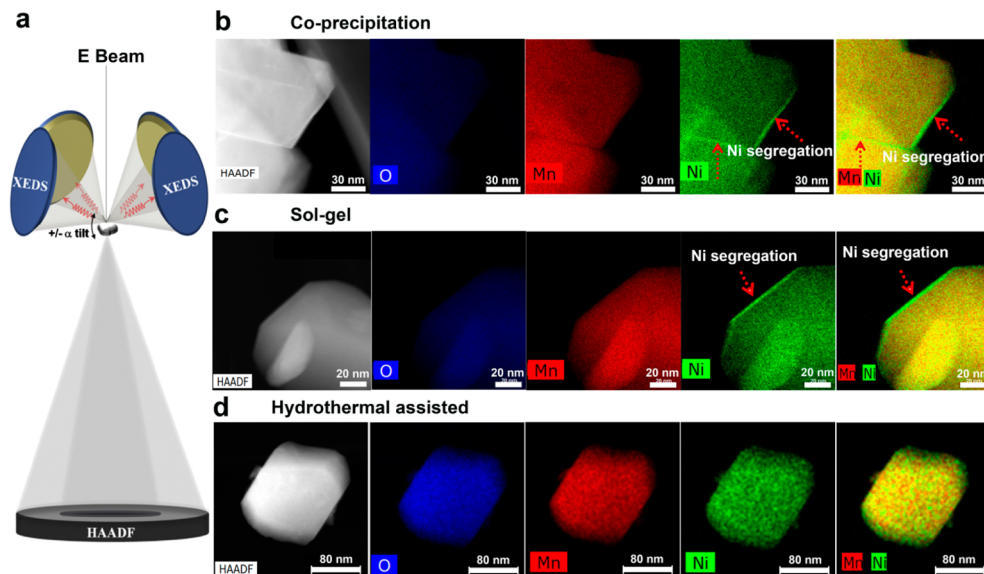


Figure 3. Z-contrast imaging and XEDS mapping of materials prepared by different methods. (a) Schematic drawing showing the newly developed four-detector system in a TEM, enabling efficient collecting of the EDS signal. Z-contrast images as well as XEDS maps of Mn, Ni, and overlaid Mn/Ni maps of (b) CP material, (c) SG material, and (d) HA material.

Information) despite the phase transformation, especially at the end of charge or discharge, which is superior to those observed in the CP material.³⁸ This result clearly indicates that the reversible lithium ion intercalation/deintercalation processes in the converted spinel-like phase appear to be not affected by the phase transformation, because the total discharge capacity remains unchanged. In addition, the HA material shows only a ~0.15 V decrease in average discharge voltage over 200 cycles (Figure 2c), much smaller than those observed for CP and SG materials (0.25 V). Owing to the suppressed phase transformation (less voltage fade) and the excellent structural stability for lithium ion insertion/extraction (stable capacity), the HA material exhibits an energy density of 750 Wh kg⁻¹ and almost no energy fade in 200 cycles, as shown in Figure 2d.

To determine the local chemical species in the bulk and at the surface, quantitative mapping of Mn, Ni, and O were performed on the as-prepared LMR materials using a newly developed four-detector system in a transmission electron microscope (TEM) (Figure 3a). Figure 3b–d shows the Z-contrast image and the distributions of Mn, Ni, and O in the as-prepared Li[Ni_{0.20}Li_{0.20}Mn_{0.60}]O₂ nanoparticles. For CP material, both Mn (red) and O (blue) are uniformly distributed throughout the nanoparticles of CP material, whether inside the particle bulk or at the grain boundaries, as shown in Figure 3b. However, the distribution of Ni (green) is very uneven, with enhanced contrast in some surface regions, implying a higher concentration of Ni in these regions. The overlaid Mn/Ni maps demonstrate that the surface regions with higher contrast are rich in Ni element, which is further proven by the energy dispersive spectroscopy (EDS) line scan result as presented in Figure S3 in the Supporting Information. The result clearly indicates that the concentration of Ni is much higher (more than double) at the particle surface than in the grain bulk. A similar nonuniform Ni distribution is also observed from EDS mapping on other particles of CP material (Figure S4 in the Supporting Information). This observation of nonuniform Ni distribution, which is a very unexpected phenomenon, is consistent with those reported previously by Gu et al.³⁰ Ideally, a homogeneous distribution of TM ions in the CP process (see

Supporting Information) should lead to LMR cathodes with uniform element distributions.³⁹ However, the distribution of Ni/Mn in the mixed hydroxide M(OH)₂ was affected by several experimental parameters such as pH value, stirring speed, temperature, and reaction atmosphere. Local variation of these parameters may affect the migration of different species and the Ni distribution in the CP material.^{38,39} Another negative effect of the formation of Ni-rich particle surface is related to more prominent surface instabilities. A high concentration of highly reactive Ni⁴⁺ ions at the particle surface will react with electrolyte at high voltages (>4.4 V), which in turn severely deteriorates the electrode/electrolyte interface after repeated cycling.^{6,40} During cycling at C/5, the CP material retains only 66.2% of its original discharge capacity after 200 cycles.

Similar to the CP material, the SG material also shows apparent nonuniform Ni distribution on the particle surface and grain boundaries, as revealed by the quantitative EDS mapping shown in Figure 3c and Figure S5 in the Supporting Information. It is possible that the nonuniform Ni distribution in the SG material originates from the gel drying process, in which the Mn citrate chelate and Ni citrate chelate may separate from each other. The degree of nonuniform Ni distribution appears to be somewhat less than that in the CP material, probably due to improved cation distribution during the SG synthesis. The Ni signal contrast between the particle surface and the particle bulk in the SG material is less than that found in the CP material (Figure S5). The discharge capacity of the SG material at the 2 C rate is 149 mAh g⁻¹, which is higher than 135 mAh g⁻¹ for the CP material, as shown in Figure 1b. The capacity retention of SG material is increased to 72.8% after 200 cycles, better than that of CP material.

In contrast to those observed in the CP and SG materials, all elements, including O, Mn, and Ni, in the as-prepared HA material are uniformly distributed, demonstrating significantly enhanced uniformity of Ni distribution at the particle surface as representatively illustrated in Figure 3d and Figures S6, S7 in the Supporting Information. To further verify the uniform Ni distribution in the HA material, NanoSIMS (second day ion mass spectrometer) measurements were carried out to probe the Ni

distribution on both surface and inside of the particles for the three samples. The SIMS data further confirms the uniform Ni distribution in the particles of the HA material, as proved by the much more uniform NiO/MnO signal ratio across the HA particle as compared to the large variation of NiO/MnO signal ratio from surface to inside of CP particle (Figure S8 in the Supporting Information). As the calcination process for HA material is the same as those used for CP and SG materials, the even distribution of Ni/Mn in the HA material would have been formed during the hydrothermal processing. The significantly improved uniformity of Ni distribution leads to the excellent electrochemical performance of HA material, which exhibits good rate capability (Figure 1b), excellent cycling stability (Figure 1c), and significantly mitigated voltage and energy fade (Figure 2c and d). The suppressed formation of Ni-rich particle surface can also explain the discrepancy between CP/SG and HA materials in terms of charge capacity below 4.45 V.

To further gain insight into the atomic-scale crystal structure difference of materials prepared by different methods, we further used aberration-corrected STEM to probe the atomic structures of the CP material and the HA material. The atomic level crystal structures of the CP material are shown in Figure 4. Similar to those reported previously, the CP material is composed of two components as presented in Figure 4a-d: trigonal LiMO_2 $R\bar{3}m$ ($\alpha\text{-NaFeO}_2$ structure) and monoclinic Li_2MO_3 type $C2/m$ phase, both of which comprise repeating

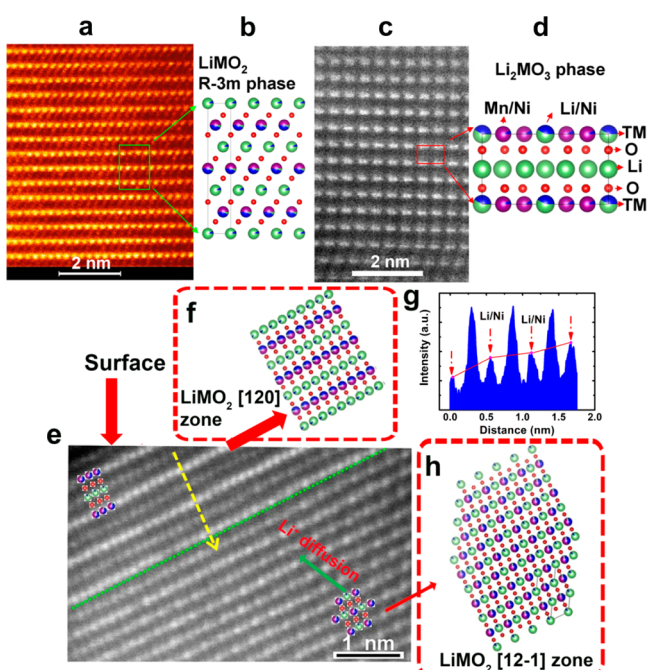


Figure 4. STEM imaging of fresh CP material. (a) Crystal structure of $R\bar{3}m$ phase; (b) atomic model of the $R\bar{3}m$ phase in the [100] zone projection, which corresponds to the green rectangle in panel (a); (c) crystal structure of $C2/m$ phase; (d) atomic model of the $C2/m$ phase in the [100] zone projection, which corresponds to the red rectangle in panel (c). (e) Atomic-scale Z-contrast image showing the Ni-rich induced surface modification. Note that the upper left region above the green dashed line is the Ni-rich region; its atomic model (f) corresponds to the [120] zone projection of the LiMO_2 $R\bar{3}m$ phase, and the intensity plot along the yellow arrow is shown in (g); the bottom right region corresponds to the [12-1] zone projection of the LiMO_2 $R\bar{3}m$ phase, and the corresponding model is presented in (h).

stacks of the lithium layer, oxygen layer, and TM layer.^{16,30,32,41} Figure 4b and d represents the atomic model of the LiMO_2 $R\bar{3}m$ structure and Li_2MO_3 type $C2/m$ structure in the [100] zone projection, respectively. Although Li_2MO_3 $C2/m$ phase could also be identified among different regions of the particle as presented in Figure 4c and d, most regions of the particle adopt the $R\bar{3}m$ $\alpha\text{-NaFeO}_2$ structure where the TM layer has the highest contrast in the HAADF Z-contrast image as shown in Figure 4a and b. This result is consistent with the previous reports that the pristine $\text{Li}[\text{Li}_{0.2}\text{Ni}_{0.2}\text{Mn}_{0.6}]_2\text{O}_2$ prepared by the CP method can be regarded as a single phase with “composite structure”^{41,42} which will gradually transform to the spinel-like structure during cycling.²⁰ Moreover, it is worth noting that the structure of conventional layered material with a $R\bar{3}m$ $\alpha\text{-NaFeO}_2$ structure (e.g., $\text{LiNi}_{0.5}\text{Mn}_{0.5}\text{O}_2$) is unstable under excessive lithium ion removal and shows fast capacity degradation at charge voltage higher than 4.4 V.³⁶ The dominance of $R\bar{3}m$ phase in Ni-segregated materials could be one of the reasons for their fast voltage fade and poor cycling stability.

In addition, Figure 4e-h shows the atomic structure of the LiMO_2 surface region. At outer surface region, a surface capping layer (~3 nm) corresponding to the [120] zone projection of the LiMO_2 $R\bar{3}m$ phase (Figure 4f) is formed ascribed to the preferential segregation of Ni ions, which leads to the termination of the particle facet with TM ions. The contrast line profile in Figure 4g shows that the intensity of Li/Ni sites (where Li is partially replaced by Ni, as indicated with red arrow in Figure 4g) increases monotonously along the yellow arrow in Figure 4e, indicating an increase of Ni in these planes, thus leading to the structural rearrangement at inner region. The inner surface region corresponds to the [12-1] zone projection of the LiMO_2 $R\bar{3}m$ phase, and the corresponding model is shown in Figure 4h, where Li ion diffusion is along the Li channels as pointed by the green arrow in Figure 4e. However, the fast lithium ion diffusion channels inside the particle are approximately perpendicular to the channels within the outer surface layer formed on the nanoparticle. Therefore, the formation of this surface capping layer leads to a largely increased diffusion barrier for Li ions at the particle surface region and has a direct impact on the rate performance of the LMR material.

The atomic resolution structure of the HA material as probed by aberration-corrected STEM is presented in Figure 5. Electron energy loss spectroscopy (EELS) data confirms the existence of both Ni and Mn in this region (Figure S9 in the Supporting Information). The atomic structure of the HA material is significantly different from that of the CP material. The surface region of the HA material shows a uniform contrast compared to its inner region, indicating nonuniform Ni distribution is greatly reduced or eliminated. The red arrows indicate the termination plane as (010) in most surface regions, as shown in Figure 5a. The atomic-scale image in Figure 5a-b shows that the region with yellow lines matches the atomic model of the Li_2MO_3 type $C2/m$ phase in the [100] zone axis projection, while the region with green line matches the atomic model of the $C2/m$ phase in the [1-10] zone projection. The plotted intensity scan in Figure 5d from the red line labeled in Figure 5b shows that the nearest atomic column distance in the [100] projection is around 0.14 nm and the centers of the atomic dumbbells are around 0.42 nm apart. The most important feature we found in the HA material is that the $C2/m$ structure becomes dominant in most regions of the

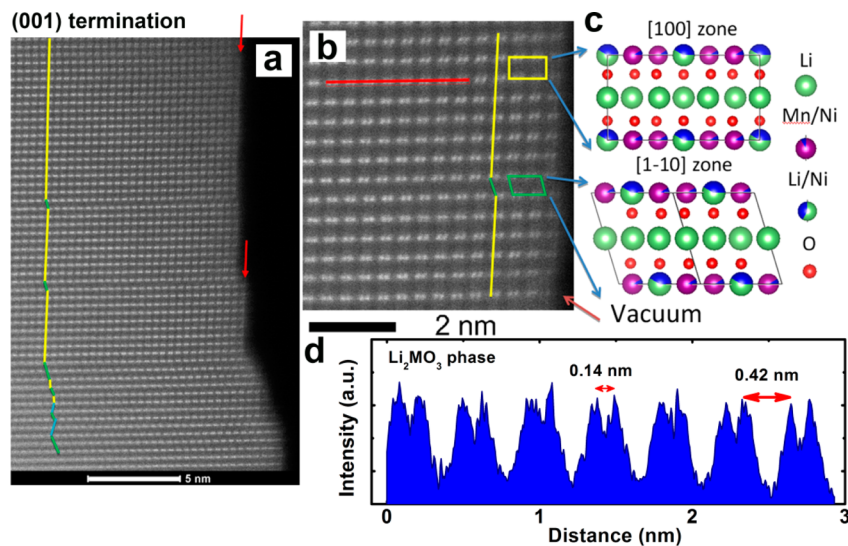


Figure 5. STEM imaging of the fresh HA material. (a) Atomic-scale Z-contrast image showing the mixed growth of different zone axes of the $C2/m$ phase; (b) higher magnification Z-contrast image showing the mixed [100] (yellow) and [1-10] zone (green); (c) atomic model showing the atomic arrangement of the $C2/m$ phase in [100] and [1-10] zone projections; (d) intensity plot along the red line shown in panel (b). Note that the termination plane of the crystal is indexed as (010) plane.

particles due to the homogeneous cation distribution, while the $R\bar{3}m$ phase could hardly be identified, which is quite different from the structures found for CP materials in which most of the regions adopt $R\bar{3}m$ phase. On this basis, the HA material could be considered as a kind of solid solution with $C2/m$ monoclinic symmetry ($x = 0.2$ of $\text{Li}[\text{Li}_{(1/3-2x/3)}\text{Ni}_x\text{Mn}_{(2/3-x/3)}]\text{O}_2$). These observations shed light on the current debate regarding the average/local structure of LMR cathode materials.^{41,43} Whether $\text{Li}[\text{Li}_{0.2}\text{Ni}_{0.2}\text{M}_{0.6}]\text{O}_2$ material is primarily a trigonal $R\bar{3}m$ phase with Li_2MnO_3 -like components or a solid solution with $C2/m$ monoclinic symmetry and multiple planar defects is closely related to the synthesis method and preparation conditions. This could be one of the most important reasons behind the largely different observations reported by different groups on the crystal structure of $\text{Li}[\text{Li}_{0.2}\text{Ni}_{0.2}\text{M}_{0.6}]\text{O}_2$ material.

In addition to the nonuniform Ni distribution at the particle surface, materials prepared by the CP and SG methods tend to form two-phase coexistent structure similar to those prepared by the solid-state reaction method.⁴¹ In contrast, the HA method leads to more homogeneous distribution of the chemical species in the particles, which favors the formation of $C2/m$ -phase dominant structure along with diminished Ni-rich particle surface.

As compared to CP and SG materials, the fast lithium ion diffusion pathways in HA material are not blocked by the Ni-rich surface layer.³⁰ The lower concentration of Ni at the particle surface also reduces side reactions between highly active Ni^{4+} and the electrolyte upon charge to high voltages, which keeps the electrode/electrolyte interface stable for reversible lithium ion intercalation/deintercalation. The formation of dominating Li_2MO_3 type $C2/m$ structure ($M = \text{Ni}/\text{Mn}$) makes the HA material more stable in case of excessive lithium ion removal, therefore significantly enhancing the cycle life and suppressing the voltage fade of HA material. Our results are strongly supported by Thackeray et al.'s recent findings that nickel–manganese interactions play an important role in maintaining the average oxidation state of the manganese ions above 3+, even for a relatively high Mn concentration.^{44–46} Significant nonuniform Ni distribution at atomic level will

weaken nickel–manganese interactions, leading to easy reduction of the manganese ions and fast voltage/capacity fade. In contrast, uniform distribution of Ni at atomic level is beneficial for enhancing the Ni–Mn interactions and will stabilize the crystal structure of $\text{Li}[\text{Li}_{0.2}\text{Ni}_{0.2}\text{M}_{0.6}]\text{O}_2$ material.

In summary, we have found that the voltage fade and energy degradation of LMR cathode materials can be significantly mitigated by improving the uniformity of chemical species at atomic level. Although many factors including the synthesis method, Li/Ni cation mixing, electrolyte component, and testing conditions may also affect the electrochemical properties of LMR cathode, a homogeneous cation distribution at atomic level is critical for stable operation of the LMR cathode. Otherwise, the degradation from intrinsic structural change will be accelerated as well as introducing other defects to induce nonuniform Ni distribution during cycling. The results also shed light on the current debate regarding the average/local structure of LMR cathode materials. LMR cathodes with significant nonuniform Ni distribution are dominated by the $R\bar{3}m$ phase, where the preferential segregation of Ni blocks lithium ion diffusion channels and weakens nickel–manganese interactions, leading to easy reduction of the manganese ions and fast voltage/capacity fade. In contrast, LMR cathodes with ameliorated Ni distribution tend to form a kind of solid solution dominated by Li_2MO_3 type $C2/m$ monoclinic structure, which is more stable against excessive lithium ion removal, oxygen release, and the parasitic side reactions between the cathode electrode and the electrolyte. The homogeneous cation distribution also enhances Ni–Mn interaction and stabilizes crystal structure, therefore leading to greatly reduced voltage fade and excellent cycling stability of LMR cathodes. Therefore, LMR cathodes with uniform distribution of chemical species (minimal Ni-rich surface) are very promising for use in high energy density Li-ion batteries for large-scale practical applications. The fundamental correlation between the atomic level spatial distribution of the chemical species and the functional stability of the materials found in this work also provides new perspective on the design

and development of other functional materials with significantly enhanced stability.

■ ASSOCIATED CONTENT

Supporting Information

Experimental details of material synthesis and characterization; supporting electrochemical data; XEDS mapping and the corresponding quantitative line scan data; NanoSIMS and EELS data. This material is available free of charge via the Internet at <http://pubs.acs.org>.

■ AUTHOR INFORMATION

Corresponding Authors

*E-mail: Chongmin.wang@pnnl.gov (C.-M. Wang).

*E-mail: Jiguang.zhang@pnnl.gov (J.-G. Zhang).

Author Contributions

J. Zheng and M. Gu contributed equally to this work.

Notes

The authors declare no competing financial interest.

■ ACKNOWLEDGMENTS

This work is supported by the Assistant Secretary for Energy Efficiency and Renewable Energy, Office of Vehicle Technologies of the U.S. Department of Energy under Contract No. DE-AC02-05CH11231, Subcontract No. 18769, under the Batteries for Advanced Transportation Technologies program. The microscopic study described in this paper is supported by the Laboratory Directed Research and Development Program as part of the Chemical Imaging Initiative at Pacific Northwest National Laboratory (PNNL). The work was conducted in the William R. Wiley Environmental Molecular Sciences Laboratory (EMSL), a national scientific user facility sponsored by DOE's Office of Biological and Environmental Research and located at PNNL. PNNL is operated by Battelle for the DOE under Contract DE-AC05-76RLO1830. The authors also would like to thank M. M. Thackeray for useful discussions.

■ REFERENCES

- (1) Tarascon, J. M.; Armand, M. *Nature* **2001**, *414*, 359–367.
- (2) Chan, C. K.; Zhang, X. F.; Cui, Y. *Nano Lett.* **2007**, *8*, 307–309.
- (3) Goodenough, J. B.; Abruna, H. D.; Buchanan, M. V.; Visco, S.; Whittingham, M. S.; Dunn, B.; Gogotsi, Y.; Gewirth, A.; Nocera, D. Basic Research Needs for Electrical Energy Storage. Report of the Basic Energy Sciences Workshop on Electrical Energy Storage, April 2–4, 2007; http://web.anl.gov/energy-storage-science/publications/EES_rpt.pdf.
- (4) Kim, D. K.; Muralidharan, P.; Lee, H.-W.; Ruffo, R.; Yang, Y.; Chan, C. K.; Peng, H.; Huggins, R. A.; Cui, Y. *Nano Lett.* **2008**, *8*, 3948–3952.
- (5) Park, M.-H.; Kim, M. G.; Joo, J.; Kim, K.; Kim, J.; Ahn, S.; Cui, Y.; Cho, J. *Nano Lett.* **2009**, *9*, 3844–3847.
- (6) Sun, Y.-K.; Myung, S.-T.; Park, B.-C.; Prakash, J.; Belharouak, I.; Amine, K. *Nat. Mater.* **2009**, *8*, 320–324.
- (7) Yang, Y.; Xie, C.; Ruffo, R.; Peng, H.; Kim, D. K.; Cui, Y. *Nano Lett.* **2009**, *9*, 4109–4114.
- (8) Armstrong, A. R.; Lyness, C.; Panchmatia, P. M.; Islam, M. S.; Bruce, P. G. *Nat. Mater.* **2011**, *10*, 223–229.
- (9) McDowell, M. T.; Lee, S. W.; Ryu, I.; Wu, H.; Nix, W. D.; Choi, J. W.; Cui, Y. *Nano Lett.* **2011**, *11*, 4018–4025.
- (10) Yao, Y.; McDowell, M. T.; Ryu, I.; Wu, H.; Liu, N.; Hu, L.; Nix, W. D.; Cui, Y. *Nano Lett.* **2011**, *11*, 2949–2954.
- (11) Sun, Y.-K.; Chen, Z.; Noh, H.-J.; Lee, D.-J.; Jung, H.-G.; Ren, Y.; Wang, S.; Yoon, C. S.; Myung, S.-T.; Amine, K. *Nat. Mater.* **2012**, *11*, 942–947.
- (12) Whittingham, M. S. *Proc. IEE* **2012**, *100*, 1518–1534.
- (13) Lu, Z.; Dahn, J. R. *J. Electrochem. Soc.* **2002**, *149*, A815–A822.
- (14) Kang, S. H.; Amine, K. *J. Power Sources* **2005**, *146*, 654–657.
- (15) Thackeray, M. M.; Johnson, C. S.; Vaughn, J. T.; Li, N.; Hackney, S. A. *J. Mater. Chem.* **2005**, *15*, 2257–2267.
- (16) Armstrong, A. R.; Holzapfel, M.; Novák, P.; Johnson, C. S.; Kang, S.-H.; Thackeray, M. M.; Bruce, P. G. *J. Am. Chem. Soc.* **2006**, *128*, 8694–8698.
- (17) Thackeray, M. M.; Kang, S.-H.; Johnson, C. S.; Vaughn, J. T.; Benedek, R.; Hackney, S. A. *J. Mater. Chem.* **2007**, *17*, 3112–3125.
- (18) Yabuuchi, N.; Yoshiii, K.; Myung, S.-T.; Nakai, I.; Komaba, S. *J. Am. Chem. Soc.* **2011**, *133*, 4404–4419.
- (19) Sun, Y.-K.; Lee, M.-J.; Yoon, C. S.; Hassoun, J.; Amine, K.; Scrosati, B. *Adv. Mater.* **2012**, *24*, 1192–1196.
- (20) Gu, M.; Belharouak, I.; Zheng, J.; Wu, H.; Xiao, J.; Genc, A.; Amine, K.; Thevuthasan, S.; Baer, D. R.; Zhang, J.-G.; Browning, N. D.; Liu, J.; Wang, C. *ACS Nano* **2013**, *7*, 760–767.
- (21) Johnson, C. S.; Kim, J. S.; Lefief, C.; Li, N.; Vaughn, J. T.; Thackeray, M. M. *Electrochim. Commun.* **2004**, *6*, 1085–1091.
- (22) Lee, D. K.; Park, S. H.; Amine, K.; Bang, H. J.; Parakash, J.; Sun, Y. K. *J. Power Sources* **2006**, *162*, 1346–1350.
- (23) Lim, J.-H.; Bang, H.; Lee, K.-S.; Amine, K.; Sun, Y.-K. *J. Power Sources* **2009**, *189*, 571–575.
- (24) Deng, H.; Belharouak, I.; Sun, Y.-K.; Amine, K. *J. Mater. Chem.* **2009**, *19*, 4510–4516.
- (25) Choi, N.-S.; Chen, Z.; Freunberger, S. A.; Ji, X.; Sun, Y.-K.; Amine, K.; Yushin, G.; Nazar, L. F.; Cho, J.; Bruce, P. G. *Angew. Chem., Int. Ed.* **2012**, *51*, 9994–10024.
- (26) Yu, H.; Zhou, H. *J. Phys. Chem. Lett.* **2013**, *4*, 1268–1280.
- (27) Zheng, J.; Gu, M.; Xiao, J.; Zuo, P.; Wang, C.; Zhang, J.-G. *Nano Lett.* **2013**, *13*, 3824–3830.
- (28) Xu, B.; Fell, C. R.; Chi, M.; Meng, Y. S. *Energy Environ. Sci.* **2011**, *4*, 2223–2233.
- (29) Zheng, J. M.; Li, J.; Zhang, Z. R.; Guo, X. J.; Yang, Y. *Solid State Ionics* **2008**, *179*, 1794–1799.
- (30) Gu, M.; Belharouak, I.; Genc, A.; Wang, D.; Wang, Z.; Amine, K.; Gao, F.; Zhou, G.; Thevuthasan, S.; Baer, D. R.; Zhang, J.-G.; Browning, N. D.; Liu, J.; Wang, C. *Nano Lett.* **2012**, *12*, 5186–5191.
- (31) Meng, Y. S.; Ceder, G.; Grey, C. P.; Yoon, W. S.; Jiang, M.; Bréger, J.; Shao-Horn, Y. *Chem. Mater.* **2005**, *17*, 2386–2394.
- (32) Bareño, J.; Lei, C. H.; Wen, J. G.; Kang, S. H.; Petrov, I.; Abraham, D. P. *Adv. Mater.* **2010**, *22*, 1122–1127.
- (33) Zheng, J. M.; Zhang, Z. R.; Wu, X. B.; Dong, Z. X.; Zhu, Z.; Yang, Y. *J. Electrochem. Soc.* **2008**, *155*, A775–A782.
- (34) Johnson, C. S.; Li, N.; Lefief, C.; Vaughn, J. T.; Thackeray, M. M. *Chem. Mater.* **2008**, *20*, 6095–6106.
- (35) Croy, J. R.; Kim, D.; Balasubramanian, M.; Gallagher, K.; Kang, S.-H.; Thackeray, M. M. *J. Electrochim. Soc.* **2012**, *159*, A781–A790.
- (36) Lin, H.; Zheng, J.; Yang, Y. *Mater. Chem. Phys.* **2010**, *119*, 519–523.
- (37) Tan, S.; Zhang, Z.; Li, Y.; Li, Y.; Zheng, J.; Zhou, Z.; Yang, Y. *J. Electrochim. Soc.* **2013**, *160*, A285–A292.
- (38) Zheng, J.; Shi, W.; Gu, M.; Xiao, J.; Zuo, P.; Wang, C.; Zhang, J.-G. *J. Electrochim. Soc.* **2013**, *160*, A2212–A2219.
- (39) Lee, M. H.; Kang, Y. J.; Myung, S. T.; Sun, Y. K. *Electrochim. Acta* **2004**, *50*, 939–948.
- (40) Woo, S.-U.; Park, B.-C.; Yoon, C. S.; Myung, S.-T.; Prakash, J.; Sun, Y.-K. *J. Electrochim. Soc.* **2007**, *154*, A649–A655.
- (41) Yu, H.; Ishikawa, R.; So, Y.-G.; Shibata, N.; Kudo, T.; Zhou, H.; Ikuhara, Y. *Angew. Chem., Int. Ed.* **2013**, *52*, 5969–5973.
- (42) Wang, D.; Belharouak, I.; Zhang, X.; Ren, Y.; Meng, G.; Wang, C. *J. Electrochim. Soc.* **2014**, *161*, A1–A5.
- (43) Jarvis, K. A.; Deng, Z.-Q.; Allard, L. F.; Manthiram, A.; Ferreira, P. J. *Chem. Mater.* **2011**, *23*, 3614–3621.
- (44) Kim, D.; Croy, J. R.; Thackeray, M. M. *Electrochim. Commun.* **2013**, *36*, 103–106.
- (45) Kim, D.; Sandi, G.; Croy, J. R.; Gallagher, K. G.; Kang, S.-H.; Lee, E.; Slater, M. D.; Johnson, C. S.; Thackeray, M. M. *J. Electrochim. Soc.* **2013**, *160*, A31–A38.

- (46) Thackeray, M. M.; Croy, J. R.; Trahey, L.; Pol, V.; Balasubramanian, M.; Gallagher, K. G.; J. Wen, M. K.; Chan, M. K. Y.; Kirklin, S. A.; Miller, D.; Wolverton, C. International Battery Association Meeting, Barcelona, Spain, March 10–15, 2013.